Chain Reorientation in Poly(tetrafluoroethylene) by Mobile Twin-Helix Reversal Defects

M. Kimmig, G. Strobl,* and B. Stühn

Fakultät für Physik, Universität Freiburg, Hermann-Herder-Strasse 3, 79104 Freiburg, Germany

Received September 29, 1993[⊗]

ABSTRACT: Analysis of measurements of the static scattering function by electron and X-ray diffraction, of the dynamic scattering law by neutron scattering, and of infrared and Raman spectra points at the important role of twin helix-reversal defects for the molecular dynamics in the intermediate phase and high-temperature phase (modifications IV and I) of poly(tetrafluoroethylene). In contrast to single helix-reversal defects, these twin defects constitute a local perturbation which can move along the chain without affecting remote units. One species, the "coherent" twin defect, possesses a particularly low formation energy, since it retains the twist long-range order along the chain. Formation of the defects occurs mainly in the intermediate phase. In the high-temperature phase a saturation is observed. The steep increase in the defect concentration in the intermediate phase followed by the equilibration in the high-temperature phase can be understood as a transition between a disordered state controlled by intra- and intermolecular forces to one which is only determined by the intramolecular potentials. In spite of the disorder in the helices, an orientational short-range order is retained for sequences in adjacent chains. The degree of order is related to the defect concentration. The reorientation of the CF_2 group resulting from the formation and motion of the twin defects occurs with rates in the range of 10–100 GHz. Orientational short-range order leads to a slowing down.

Introduction

Poly(tetrafluoroethylene) (PTFE) in the crystalline state exhibits a specific phase behavior.[1,2] Crystals are well ordered below T = 19 °C. At this temperature a solid–solid phase transition occurs, which is associated with the onset of internal motion. It is followed by a second phase transition at 30 °C. Both phase transitions result in a steplike increase of disorder in the crystals. In the low-temperature phase the conformation of the molecules can be described in good approximation as a 13/6 helix. The conformation in the high temperature phases is slightly different, corresponding to a 15/7 helix.[3] The three phases are usually denoted as modification II (low-temperature phase), modification IV (intermediate phase), and modification I (high-temperature phase).[4]

The mechanisms of motion active in the intermediate and the high-temperature phase and the resulting disorder structure have been discussed for a long time. The low-temperature phase is built up of arrays of right- and left-handed helices in regular order.[5–7] This order gets lost at the first phase transition; right- and left-handed helices become mixed. The mixing appears to be achieved through the action of helix-reversal defects.[8–11] These defects are thermally activated in the intermediate and the high-temperature phase and enable a transformation of a right-handed helix into a left-handed one and vice versa. Evidence for the occurrence of helix-reversal defects comes from IR spectroscopic studies and X-ray diffraction experiments. Further modes of motion discussed in the literature are screw motions of the helices,[2,12] as well as librations of helical sequences associated with large angular displacements.

A quite unusual consequence of the plastically crystalline nature of PTFE in its high-temperature phase has been reported recently.[13] If a bar of solid PTFE is moved under weak pressure against a surface, for example of a glass slide, an ultrathin layer becomes deposited. Crystallites in this partially crystalline thin film show a perfect uniform orientation, the chains being directed along the rubbing direction. In an electron-diffraction experiment single-crystal-like patterns are obtained. Temperature-dependent studies on these ultrathin films enable a precise judgement of the changes of Bragg reflection intensities as well as of the distribution of diffuse scattering at the phase transitions. This provides an excellent basis for a

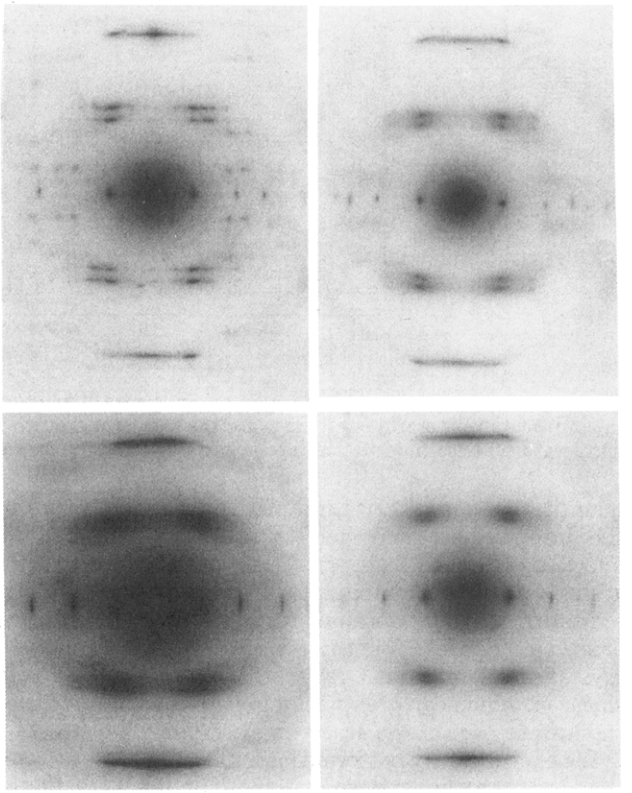

Figure 1. Thin film of PTFE prepared by the rubbing procedure. Electron diffraction patterns measured in the low-temperature phase at −25 °C (upper left), the intermediate phase at 25 °C (upper right), and the high-temperature phase at 40 °C (lower left) and 80 °C (lower right). Intensities are not comparable due to different film thicknesses and exposure times. The isotropic strong scattering in the center originates from the primary beam.

* Author to whom correspondence should be addressed.

⊗ Abstract published in *Advance ACS Abstracts,* March 15, 1994.

0024-9297/94/2227-2481$04.50/0

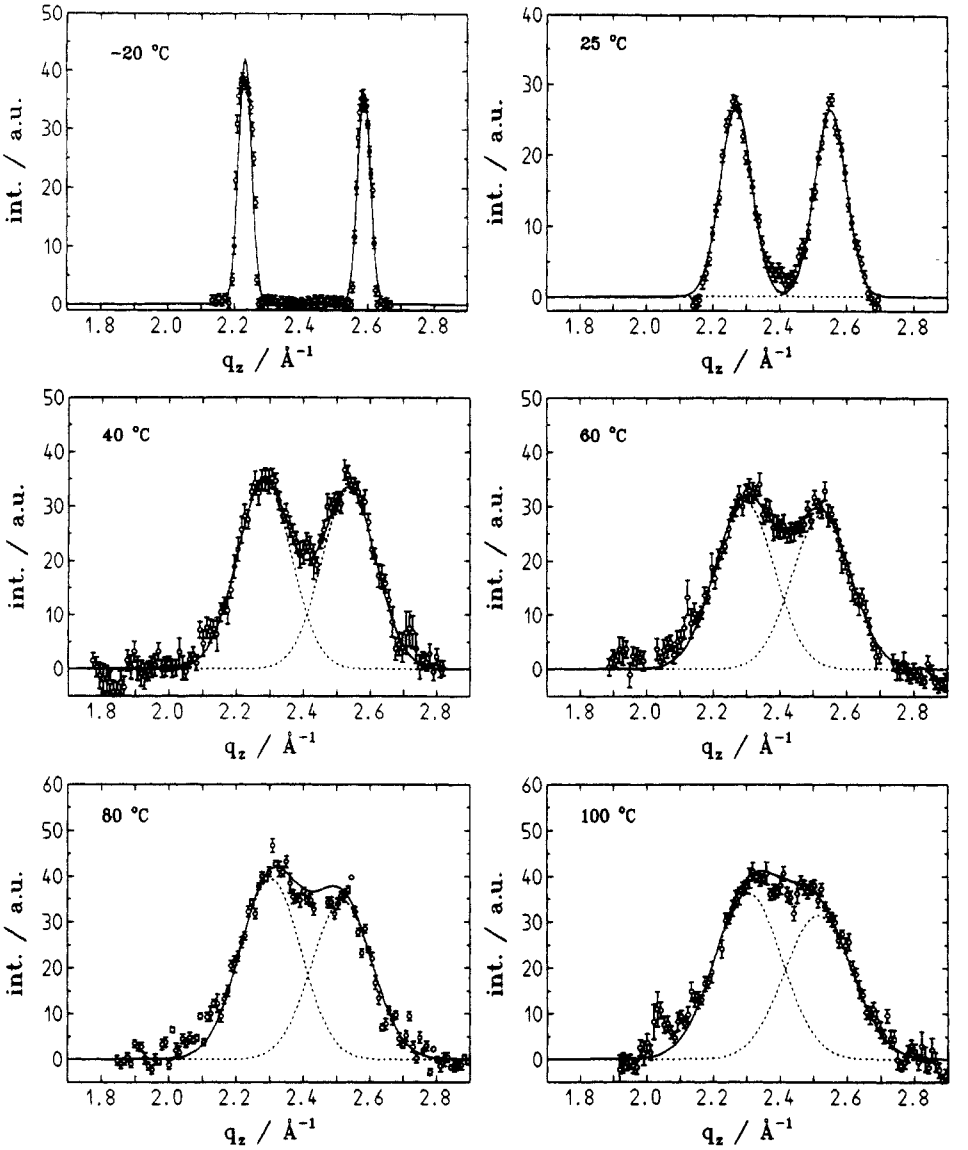

Figure 2. Intensity distributions along q_z in the torus range (q_ρ = 1.30 Å^{-1}), derived from electron diffraction patterns measured at the indicated temperatures. Results for the low-temperature phase (upper left), the intermediate phase (upper right), and the high-temperature phase (middle and lower part).

quantitative characterization of the defect structure in the intermediate and high-temperature phase. The knowledge derived from an inspection of EM diffractograms can also contribute to the evaluation of X-ray scattering diagrams obtained for cold-drawn PTFE films of normal thickness. For these films, due to an uncomplete crystallite orientation, X-ray scattering curves are usually smeared, which can greatly complicate the evaluation of the diffuse part of the scattering pattern.

We have recently performed a comprehensive study on the phase behavior and molecular dynamics of crystals of perfluoro-*n*-eicosane ($C_{20}F_{42}$).[14-17] Crystals of these oligomeric chain molecules also exhibit a plastically crystalline phase at room temperature, with a high internal mobility. Analysis of X-ray scattering patterns resulted in a clear picture of the state of motion and the disorder structure. As it turned out, the state of motion is complex and can be described as a superposition of rotations about the long axis, limited longitudinal translations, and the motion of helix-reversal defects. Rotations occur cooperatively so that an orientational short-range order is preserved. Molecular dynamics was also investigated directly by quasi-elastic neutron scattering, yielding details of the relaxation processes and their dependence on temperature.

The new experience and understanding gained in the study of the model system $C_{20}F_{42}$, together with the excellent information contained in EM diffractograms of ultrathin PTFE films, motivated us to reconsider and analyze in more detail the mechanisms of motion in the phases IV and I of PTFE. In particular, the properties of the helix-reversal defects were investigated more closely. As in the case of oligomers, studies included static X-ray and electron diffraction as well as quasi-elastic neutron-scattering experiments.

Experimental Section

The studies were conducted on a commerical PTFE, supplied by the Hoechst AG (trade name Hostaflon). Two different samples were investigated. One was a film with a thickness of 150 μm, which possessed a biaxial texture. The orientational distribution of the crystallite axes showed a halfwidth on the order of 30–40°. As a second sample an ultrathin film was studied. This film was obtained by moving a piece of PTFE against a hot glass surface (at 250 °C) and applying a weak pressure. By this procedure a film with a thickness of several 10 nm becomes deposited on the surface. Crystallites in this film show a perfect uniform orientation. The chain axis is directed along the moving direction; one of the crystallite axes is parallel to the film surface.

These ultrathin films were transferred onto a copper net for studies in an electron microscope (Philips EM 400). Diffraction

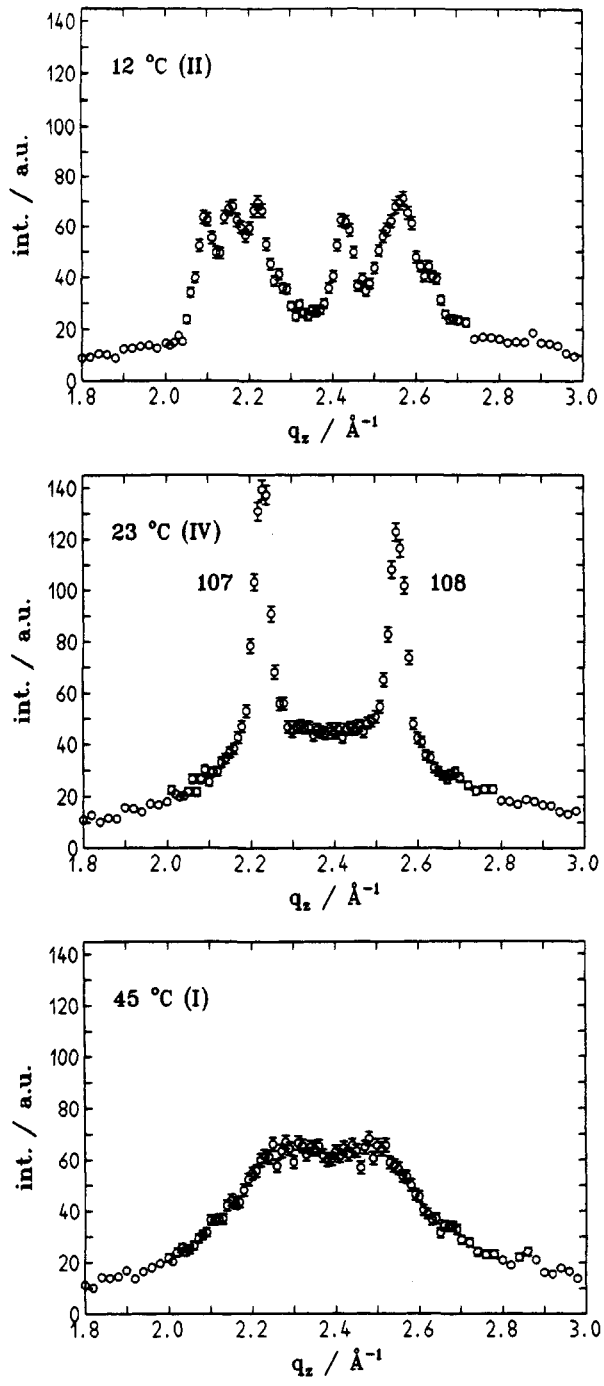

Figure 3. Thick film of PTFE with imperfect biaxial orientation. Intensity distribution of X-ray scattering in the torus range (q_z sancs at q_ρ = 1.30 Å^{-1}).

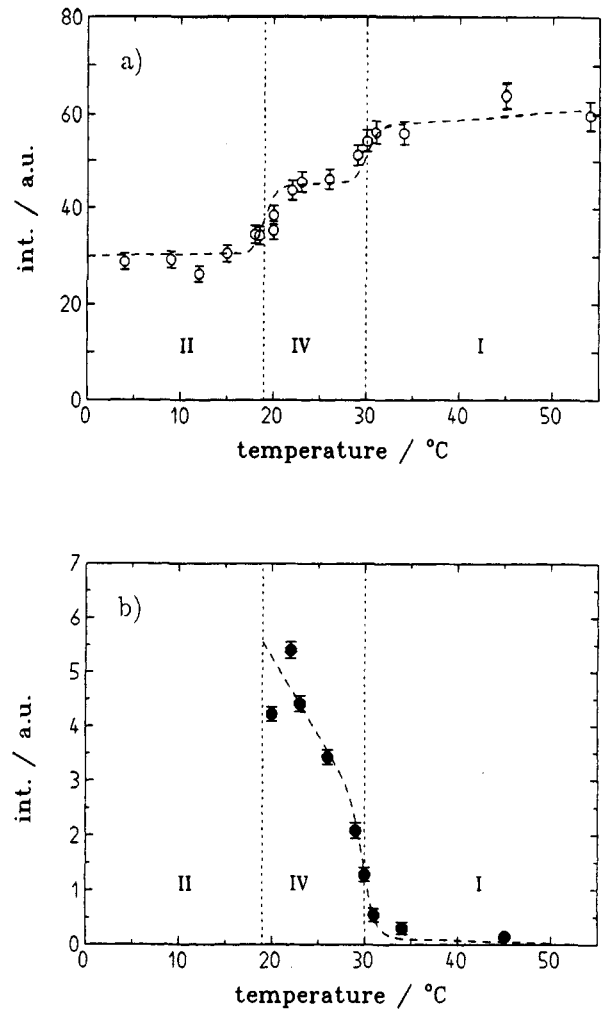

Figure 4. Measurements shown in Figure 3. Temperature dependence of the diffuse scattering intensity at q_z = 2.33 Å^{-1}, q_ρ = 1.30 Å^{-1} (a) and of the Bragg reflection intensity (b).

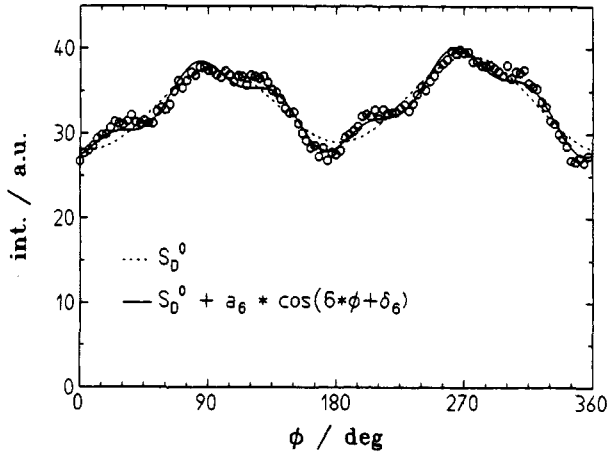

Figure 5. ϕ dependence of the diffuse scattering intensity in the torus range, registered in a X-ray scattering experiment at 36 °C for q_ρ = 1.30 Å^{-1}, q_z = 2.30 Å^{-1}.

patterns were obtained at a wavelength λ = 0.035 Å at different temperatures, using a heating stage.

Temperature-dependent measurements of the static scattering function $S(q)$ were performed on the thicker films using a X-ray Weissenberg diffractometer equipped with a scintillation counter and moved under the control of a computer (Stoe Co., Darmstadt, Germany). Cu Kα radiation from a rotating anode generator was used. The diffractometer enables the registration of the two-dimensional intensity distribution in selected reciprocal space planes.

Measurements of the dynamic scattering function $S(q,\omega)$ were performed using the spectrometer IN8 at the Institute Laue-Langevin (Grenoble, France) for inelastic measurements and the three-axes spectrometer TAS7 at the Risoe National Laboratory (Roskilde, Denmark) for quasi-elastic measurements. The spectrometer IN8 has an energy resolution of 0.35 meV, the spectrometer TAS7 a resolution of 0.25 meV.

In addition vibrational spectra were registered. Raman spectra were obtained using the spectrometer Coderg T800 together with an argon ion laser. Infrared spectra were obtained using a conventional FTIR spectrometer (Bruker Co.).

Results

Electron Diffraction. Figure 1 shows electron diffractograms obtained for an ultrathin film in the three solid phases, at −25 °C (II), 25 °C (IV), and 40 °C and 80 °C (I). The appearence of all diffractograms is single-crystal-like, indicating a perfect orientation. Three different regions with characteristic scattering behavior show up: (i) scattering at the equator; (ii) scattering in a range

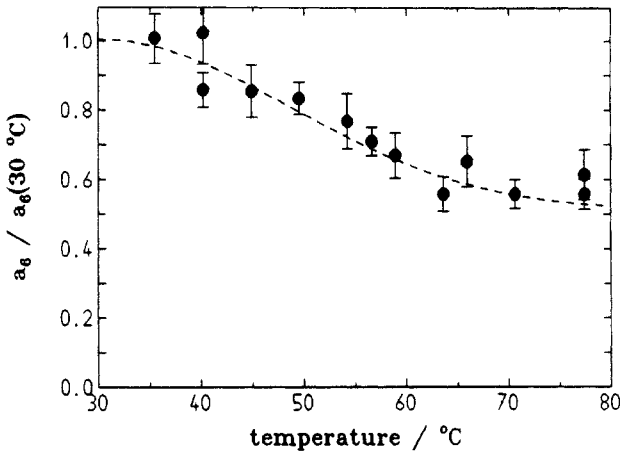

Figure 6. Temperature dependence of the amplitude a_6 of the observed modulation with period $2\pi/6$.

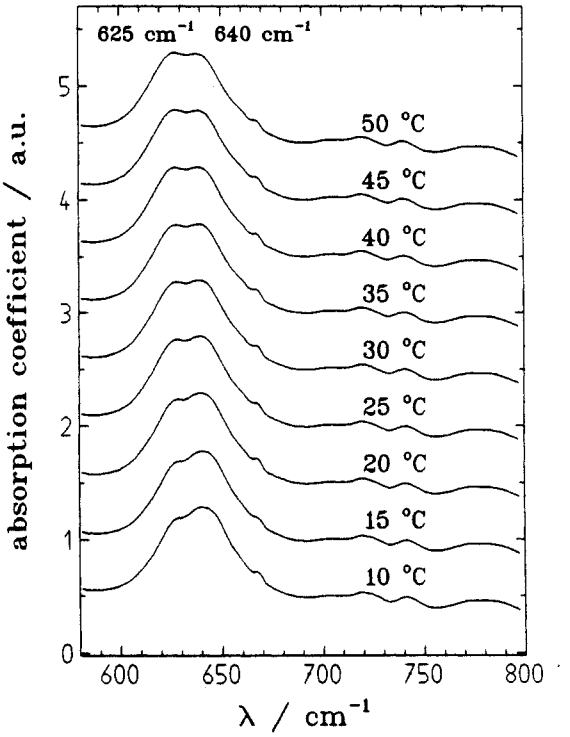

Figure 7. Infrared spectra of TPFE, registered at different temperatures in the three modifications.

of toroidal shape, denoted as "torus" range in the following, at q_z = 2.2–2.6 Å^{-1}; (iii) a layer line at $q_z = 2\pi/1.30$ Å^{-1} = 4.83 Å^{-1}, centered at the meridian.

At the equator a series of Bragg reflections exists through all phases. They are indicative for a hexagonal dense packing of the PTFE chains (strictly speaking, the packing is "pseudohexagonal" in phase II, which is triclinic).

Two layer lines contribute to the scattering in the torus range at low temperatures. They are located at $q_z = (2\pi/2.30 \pm \Delta)$ Å^{-1}. The distance 2Δ between the two layer lines decreases at the phase transition from the low-temperature phase to the intermediate phase, from 0.37 to 0.32 Å^{-1}. At this phase transition also several Bragg reflections vanish. In the intermediate phase only one Bragg reflection is left for each layer line. Diffuse streaks appear. They are oriented along the layer line, i.e., perpendicular to the chain direction. With the transition to the high-temperature phase the Bragg reflections disappear. The diffuse scattering intensity is enhanced. With increasing temperature in the high-temperature phase the layer lines show a further broadening in q_z direction. At high temperatures the two layer lines merge.

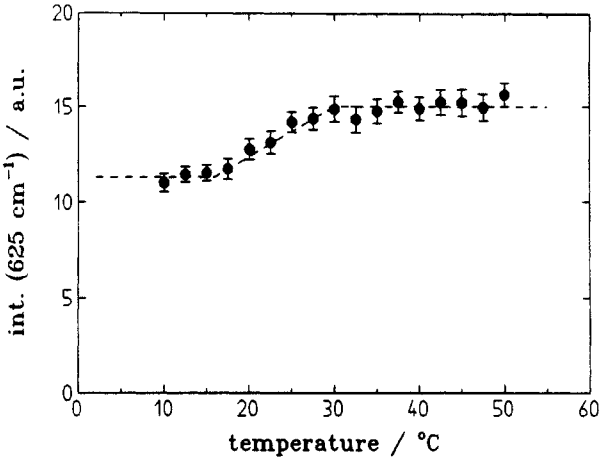

Figure 8. Temperature dependence of the intensity of the defect-induced mode at 625 cm^{-1}.

In the third region of the scattering diagram, the layer line at 4.83 Å^{-1} centered at the meridian, three Bragg reflections exist through all phases. The transition to the intermediate phase and the high-temperature phase again is associated with the appearence of diffuse streaks along the layer line.

Figure 2 shows the intensity distribution in the torus range for all phases obtained by a photometric recording. Scans were performed along q_z at a fixed q_ρ = 1.3 Å^{-1}. The curves show the decrease in the distance between the two layer lines at the II–IV phase transition and the broadening of the layer lines, with a first step at the first transition and the second step at the second transition to the high-temperature phase. The curves indicate that the merging of the two layer lines in the high-temperature phase is mostly due to a decrease in their distance.

X-ray Scattering. Figure 3 shows the corresponding results obtained for the thick-film samples with biaxial texture by X-ray scattering. Again q_z scans performed at q_ρ = 1.30 Å are given. Due to the imperfect orientation, which produces arcs rather than point-like Bragg reflections, the reflections also show up in these longitudinal scans. The observations are equivalent to those in the electron diffraction experiment: at the first transition (II → IV) some of the Bragg reflections vanish and there is an increase in the diffuse scattering. The two remaining Bragg reflections vanish at the second transition (IV → I). The two maxima observed at 45 °C correspond to the two broadened layer lines with diffuse scattering only.

Figure 4 shows the change with temperature in the diffuse scattering intensity measured at q_ρ = 1.30 Å and q_z = 2.33 Å (part a) and of the Bragg reflection intensity (b). One observes a pronounced increase of the diffuse scattering passing through the intermediate phase, together with a corresponding decrease of the Bragg reflection intensity. The X-ray scattering experiments on the thick films also made possible a determination of the azimuthal intensity distribution in the torus range. Figure 5 shows the results of a ϕ scan, performed at T = 36 °C (high-temperature phase) at q_ρ = 1.30 Å^{-1} and q_z = 2.30 Å^{-1}. The intensity distribution exhibits a 2-fold modulation. The modulation with period π is due to the varying absorption of the flat sample. The interesting point is the additional modulation with a period $2\pi/6$. The modulation amplitude, called a_6, shows a characteristic temperature dependence which is given in Figure 6. A continuous decrease with increasing temperature is observed. As will be explained later in the discussion, this modulation is indicative of correlations between the orientations of

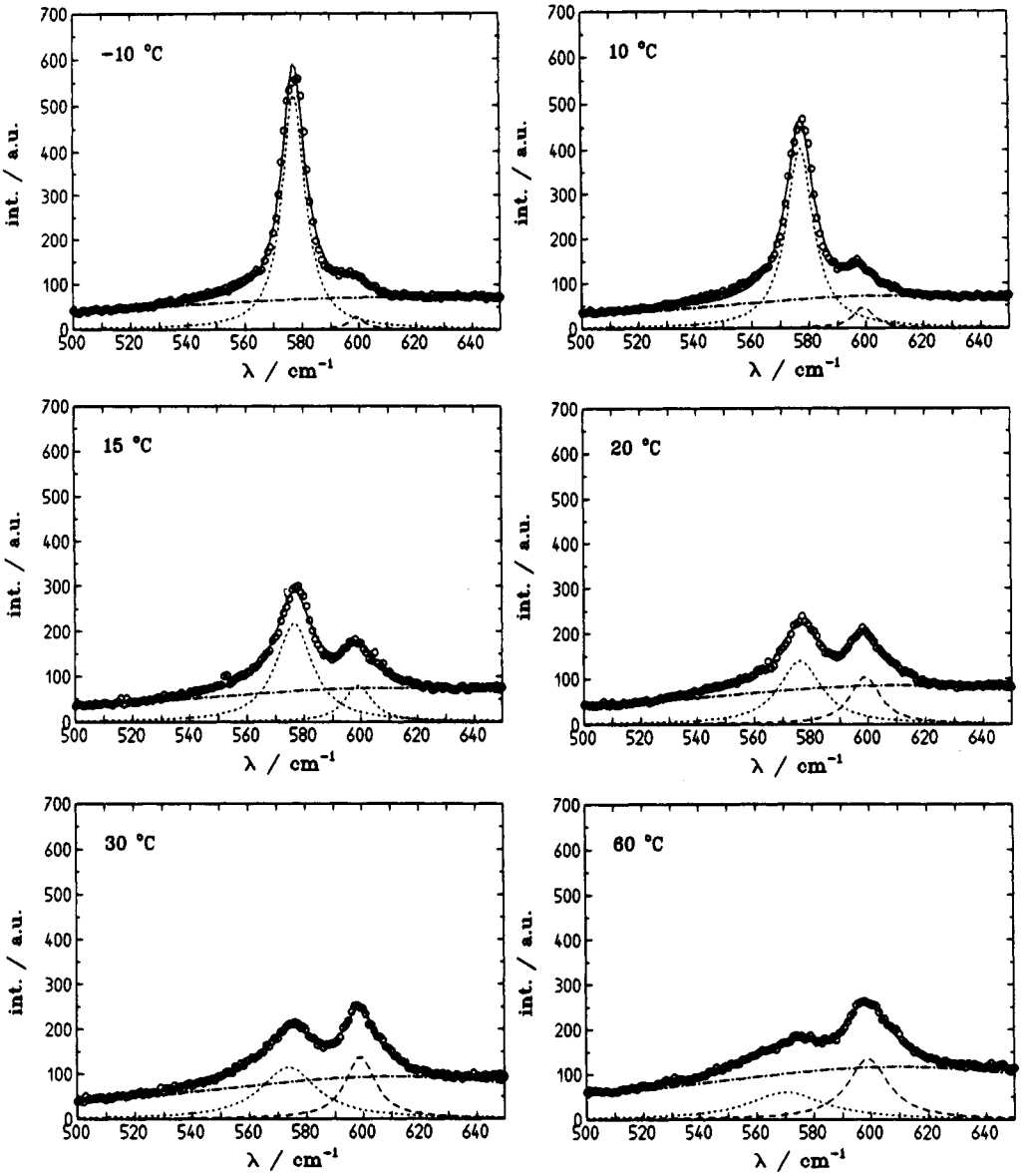

Figure 9. Raman spectra of PTFE measured at the indicated temperatures in the three modifications.

neighboring chain sequences. Figure 6 tells that correlations exist and become weaker with increasing temperature.

Vibrational Spectroscopy. Vibrational spectra are sensitive to changes in the chain conformation and therefore sensitive to the occurrence of specific local conformational states like helix-reversal defects. Figure 7 shows infrared spectra obtained at different temperatures through all three phases. As suggested first by Brown,[8] the band centered at 625 cm^{-1} reflects a local mode associated with a helix-reversal defect. Therefore, measurements of the band intensity give the temperature dependence of the concentration of the helix-reversal defect. A continuous increase with growing temperature is noted. Figure 8 gives the temperature dependence of the band intensity as it followed from a decomposition of the IR spectra. One observes a pronounced increase in the temperature range of the intermediate phase. There is also a nonvanishing contribution in the low-temperature phase, which can be associated with the coiled chain conformation in the amorphous regions in the sample.

Similar evidence is given by the Raman spectra. There is also a band, located at 598 cm^{-1}, associated with conformational defects.[18,19] Figure 9 shows Raman spectra in the different modifications. The intensity of the defect-induced band increases with temperature, whereas the band at 578 cm^{-1}, which has to be associated with unperturbed helical sequences, decreases. Figure 10 presents the temperature dependence of the defect-associated band. Again a pronounced increase is observed on passing through the intermediate phase. In contrast to the defect band in the infrared spectrum, the defect-induced Raman band shows only a low rest intensity in the low-temperature phase. Hence, the Raman-band is

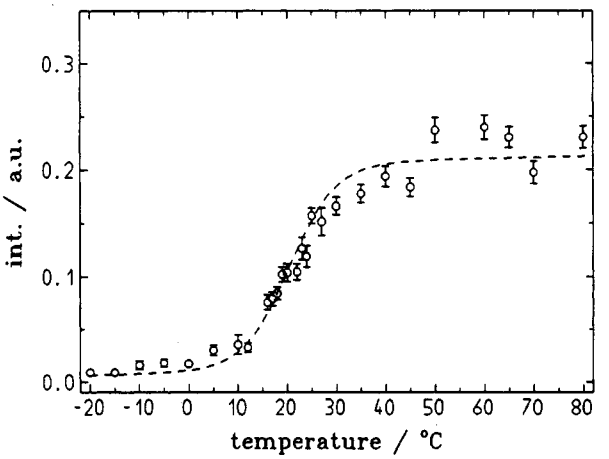

Figure 10. Temperature dependence of the intensity of the defect-induced band at 578 cm^{-1}.

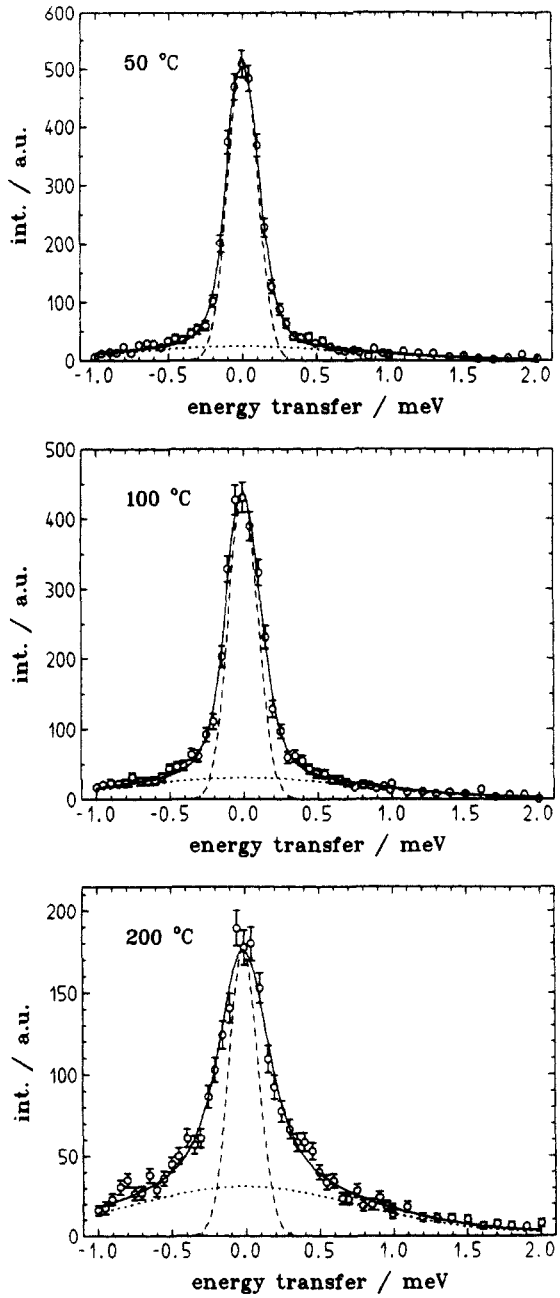

Figure 11. Dynamic structure factors measured by quasi-elastic neutron scattering in the high-temperature phase of PTFE. The narrow broken line represents the resolution function of the instrument. The dotted broad line is associated with libration modes.

more specific and possesses a high conformational selectivity. In the case of the infrared band not only helix-reversal defects give contributions. Apart from this difference, infrared and Raman spectra led to the same conclusion: there occurs a pronounced increase in the concentration of defects within the intermediate phase. Then, in the high-temperature phase a saturation is reached.

Neutron Scattering. Neutron scattering experiments were conducted on samples with biaxial texture. Samples suitable for the scattering experiments were prepared from the thick films by stacking several pieces onto each other under equal orientation. Figure 11 shows spectra obtained at three different temperatures in the high-temperature phase in the range of strong diffuse scattering in the torus region using the quasi-elastic spectrometer TAS7. The energy resolution curve is indicated. It was determined by an incoherent scattering experiment on vanadium.

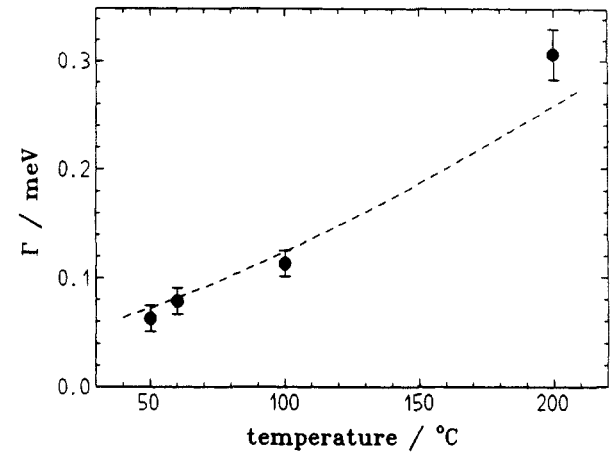

Figure 12. Temperature dependence of the width Γ of the narrow central line, derived from the spectra in Figure 11.

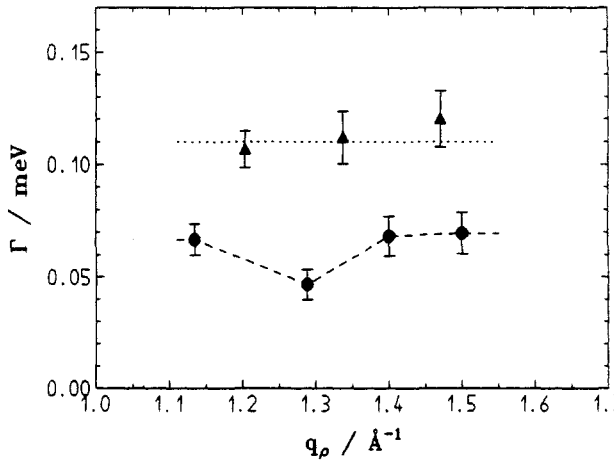

Figure 13. q_ρ dependence of the width Γ, measured at 50 °C (lower curve) and 100 °C (upper curve).

Beginning at 50 °C a line broadening is observed. In addition to the broadened center line a second contribution with a halfwidth in the order of 2 meV is observed, which originates from low-frequency vibrations. The continuous curve shows a representation of the measured spectra by a superposition of the phonon line, described by a broad Gaussian line, and a narrow Lorentz line S_L

$$S_L(\omega) \sim 1/(\omega^2 + \Gamma^2)$$

both being convoluted with the resolution function. The narrow line exhibits a quasi-elastic broadening; the linewidth Γ increases with temperature. Figure 12 shows the result of the evaluation of the spectra. As will be explained in more detail in the discussion, the torus range is sensitive for the rotational motion of chain sequences. Hence, Figure 12 indicates an increase of the rotational relaxation rate Γ with temperature.

Figure 13 shows the dependence of Γ on the location q_ρ on the layer line. For 50 °C (lower curve) a minimum shows up, being located in the region were the Bragg reflections occur in the intermediate and low-temperature phase. The minimum can be understood as a correlation-induced slowing down. The minimum might have been more pronounced in measurements of samples of perfect orientation. The orientational distribution in the samples under study leads to a smearing.

Figure 14 represents spectra obtained again in the torus range, using now an inelastic spectrometer. The broadening of the narrow line here remains unresolved. On the other hand, the phonon line can be followed over their

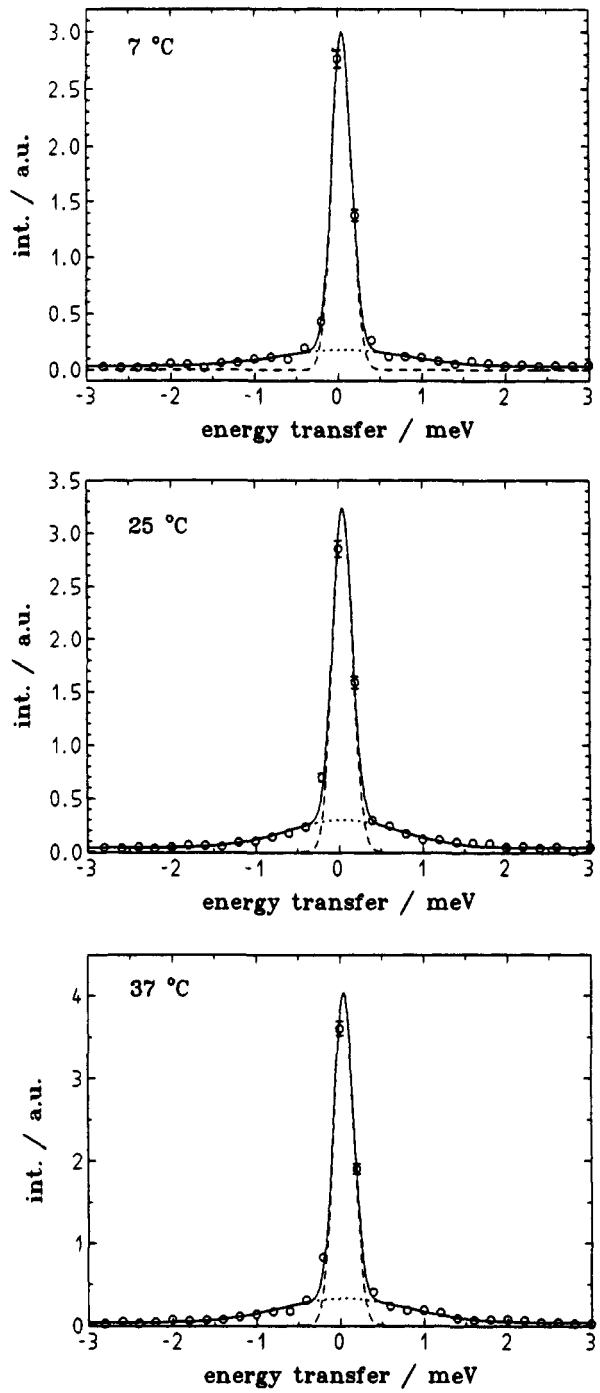

Figure 14. Dynamic structure factors measured in the torus range ($q_\rho = 1.30$ Å^{-1}, $q_z = 2.40$ Å^{-1}) by inelastic neutron scattering. The dotted broad line is associated with libration modes. The broadening of the central line observable in the spectra in Figure 11 remains unresolved.

whole width. Vibrations with such a low frequency usually are of the librational type. Obviously the frequency of the librations does not change with temperature. One observes a slight increase in intensity, i.e., the amplitude of the vibrations.

Discussion

Scattering Functions of Disordered PTFE Crystals. In order to set up a basis for the discussion of the measured scattering functions, we first collect some relevant theoretical expressions[15,20,21] concerning the scattering properties of PTFE crystals with internal disorder.

For a derivation of the structure factor of a single PTFE helix it is appropriate to introduce cylindrical coordinates in direct space and the q space, ρ, φ, z and q_ρ, ϕ, q_z, with z and q_z being oriented along the helix axis. The carbon atoms in the CF_2 units are located at

$$z_l = \Delta z \cdot l, \quad \varphi_l = \frac{t}{u} 2\pi l, \quad \rho = \rho_c = \text{constant}$$

and the fluorine atoms at

$$z_l = \Delta z \cdot l, \quad \varphi_l = \frac{t}{u} 2\pi l \pm \beta, \quad \rho = \rho_f = \text{constant}$$

with $l = 1, N$. Successive units are displaced by a shift Δz along the helix axis and a rotation by an angle $\Delta\varphi = 2\pi t/u$ (u units are distributed along t helix turns). The helix parameter t/u is 6/13 or 7/15 for the low-temperature phase or the intermediate and high-temperature phases, respectively.

Using a series expansion with Bessel functions J_k, the molecular structure factor F_m can be written as

$$F_m = \sum_{k=-\infty}^{\infty} i^k (f_c J_k(\rho_c q_\rho) + 2 f_f J_k(\rho_f q_\rho) \cos k\beta) \exp(i k\phi \cdot \sum_{l=1}^{N} \exp(i)(z_l q_z + k\varphi_l) = \sum_{k=-\infty}^{\infty} F_m{}^k \quad (1)$$

(f_c and f_f denote the atomic form factors of carbon and fluorine). Since

$$z_l q_z + k\varphi_l = l(\Delta z q_z + 2\pi k t/u) \quad (2)$$

the structure amplitude F_m shows for a long chain nonvanishing values only if

$$(\Delta z q_z + 2\pi k t/u) = n 2\pi, \; n = 0, \pm 1, \pm 2, \ldots \quad (3)$$

Equation 3 selects layer lines with contributions from associated Bessel functions J_k. The dominant contributions are usually given by J_0, J_1, J_{-1}. They are found on layer lines located at the following heights:

$$J_0\text{:} \; q_z = \frac{2\pi}{\Delta z} n \quad (4)$$

$$J_1\text{:} \; q_z = \frac{2\pi}{\Delta z} n - \frac{2\pi t}{\Delta z u} \quad (5)$$

$$J_{-1}\text{:} \; q_z = \frac{2\pi}{\Delta z} n + \frac{2\pi t}{\Delta z u} \quad (6)$$

In the limit $N \to \infty$ the layer lines become sharp.

The scattering on the equator and in the meridian range is dominated by the J_0 contribution. The intensity distribution in the torus range is essentially given by the J_1 contributions. The layer lines are located at

$$q_z = \frac{2\pi}{1.30 \text{ Å}} \cdot \frac{7}{15} = 2.26 \text{ Å}^{-1}$$

and

$$q_z = \frac{2\pi}{1.30 \text{ Å}} \left(1 - \frac{7}{15}\right) = 2.58 \text{ Å}^{-1}.$$

The equations describe helices of a given handedness. Right-handed as well as left-handed helices can be formed with equal probability. The structure factors are related

by

$$F_m^{\,l}(q_\rho,\phi,q_z) = F_m^{\,r}(q_\rho,-\phi,q_z) \tag{7}$$

(if $\phi = 0$ is chosen on the mirror plane).

For a perfect crystal, realized by a regular packing of the helices on a 2d lattice, the structure factors F_i of all unit cells are identical and equal to the molecular structure factor F_m. Internal motion results in variations of F_i between the different cells i. Variations can result from (i) longitudinal translations δ_z; (ii) rotational displacements δ_φ; (iii) a random mixing of right- and left-handed helices; (iv) the occurrence of helix-reversal defects.

A displacement δz_i of the molecule in cell i along the helix axis means $\delta z_i = \delta z_i$ for all monomers and therefore

$$F_i = \exp(i)q_z\delta z_i \cdot F_m \tag{8}$$

If the molecule is rotated about the long axis by an angle $\delta\varphi_i$, the change of F_i can also be directly given. Replacement of the azimuthal angles φ_l of the monomers by $\varphi_l - \delta\varphi_i$ results in

$$F_i = \sum_{k=-\infty}^{\infty} \exp(-i)k\delta\varphi_i \cdot F_m^{\,k} \tag{9}$$

The fluctuations originating from a disordering of the right- and left-handed helices follow from eq 7; those resulting from helix-reversal defects will be discussed separately.

The fluctuations lead to a weakening of the Bragg reflections and the appearence of diffuse scattering. The scattering function $S(\mathbf{q})$ of a disordered crystal can be generally expressed in terms of correlation functions $\langle \Delta F_i \Delta F_{i+j} \rangle$ of the fluctuations and described by a superposition of Bragg reflexions, S_B, and diffuse scattering, S_D:

$$S(\mathbf{q}) = S_B(\mathbf{q}) + S_D(\mathbf{q}) \tag{10}$$

with

$$S_B(\mathbf{q}) = |\langle F_i \rangle|^2 \sum_{hkl} \delta(\mathbf{q} - \mathbf{q}_{hkl}) \tag{11}$$

and

$$S_D(\mathbf{q}) = \sum_i \langle (F_i - \langle F_i \rangle)(F_{i+j}^* - \langle F_i \rangle^*) \rangle \exp(i)\mathbf{q}\mathbf{x}_j \tag{12}$$

$$= \sum_i \langle \Delta F_i \cdot \Delta F_{i+j}^* \rangle \exp(i)\mathbf{q}\mathbf{x}_j \tag{13}$$

($\mathbf{x}_j$ is the lattice vector connecting the unit cells i and $i + j$).

Equation 13 is usually presented in the form

$$S_D(\mathbf{q}) = \langle |\Delta F_i|^2 \rangle \cdot C(\mathbf{q}) \tag{14}$$

The function $C(\mathbf{q})$ introduced by eq 14 characterizes the short-range order and is defined by

$$C(\mathbf{q}) = \sum_j \frac{\langle \Delta F_i \Delta F_{i+j}^* \rangle}{\langle |\Delta F_i|^2 \rangle} \exp(i)\mathbf{q}\mathbf{x}_j \tag{15}$$

In case of absence of any short range order, i.e., of uncorrelated motions of the molecules, $C(\mathbf{q})$ becomes equal to unity.

Application of these equations enables an analysis of the state of disorder. Effects of different modes of motion can be discriminated, in favorable cases already by purely qualitative arguments. An example is given by the translations and rotations. They lead to different changes of the Bragg intensities

$$I_{hkl} = |\langle F_i \rangle|^2(\mathbf{q}_{hkl}) \tag{16}$$

Averaging the structure factors for varying translational shifts

$$\langle F_i \rangle = F_m \langle \exp(i)q_z\delta z_i \rangle$$

and assuming a Gaussian distribution for δz_i leads to

$$\langle \exp(i)q_z\delta z_i \rangle = \exp\left(-\frac{1}{2}\right) \langle (q_z\delta z_i)^2 \rangle \tag{17}$$

and

$$\langle F_i \rangle = \exp\left(-\frac{1}{2}\right) \langle (q_z\delta z_i)^2 \rangle \cdot F_m \tag{18}$$

Taking the average for a distribution of azimuthal turns gives

$$\langle F_i \rangle = \sum_{k=-\infty}^{\infty} \langle \exp(-i)k\delta\varphi_i \rangle F_m^{\,k} \tag{19}$$

Assuming also for $\delta\varphi_i$ a Gaussian distribution one obtains

$$\langle \exp(-i)k\delta\varphi_i \rangle = \exp\left(-\frac{1}{2}\right) \langle k^2\delta\varphi_i^{\,2} \rangle \tag{20}$$

which leads to

$$\langle F_i \rangle = \sum_{k=-\infty}^{\infty} \exp\left(-\frac{1}{2}\right) \langle k^2\delta\varphi_i^{\,2} \rangle \cdot F_m^{\,k} \tag{21}$$

In both cases, longitudinal translation and rotation, the decrease of the mean structure factors and hence of the Bragg reflection intensities is described by generalized Debye–Waller factors. A comparison shows the difference in the effects. Longitudinal translations result in a weakening which depends only on q_z and increases with q_z. Rotations, on the other hand, lead to a weakening which is only a function of q_ρ. It increases with order k of the Bessel function, which means essentially that the weakening increases with q_ρ (higher order Bessel functions have their first maximum at higher q_ρ's).

Correlations can be analyzed by an evaluation of the diffuse component S_D. Figure 15 presents as an example the result of model calculations performed for the torus range. Figure 16 shows the neighborhood of a given molecule, with three groups of next neighbors being indicated (at distances r_1, r_2, r_3).

Use of eqs 14 and 15 gives

$$S_D(q) \sim J_1^{\,2}(q_\rho \cdot r_f) \sum_j C_j \exp(i)\mathbf{q}\mathbf{x}_j$$

$$= J_1^{\,2}(q_\rho \cdot r_f) \cdot C(\mathbf{q}) \tag{22}$$

(only J_1 contributions are accounted for; the comparatively weak scattering of the carbon atoms is neglected). The summation involves all the neighbors given in Figure 16;

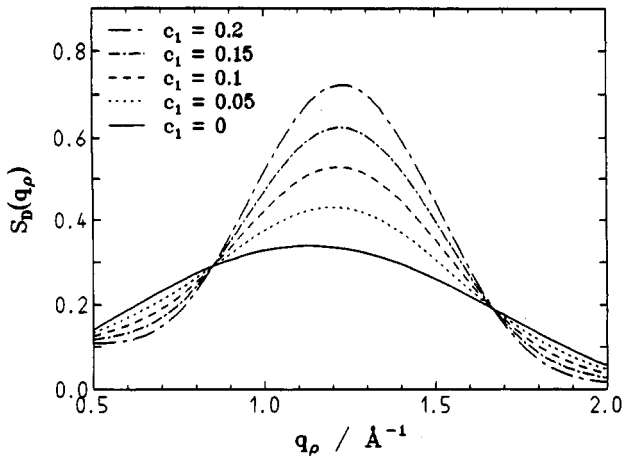

Figure 15. Effect of correlations in the rotational motion of neighboring sequences on the intensity distribution of the diffuse scattering in the torus range. Result of model calculations assuming different values of the correlation coefficient C_1.

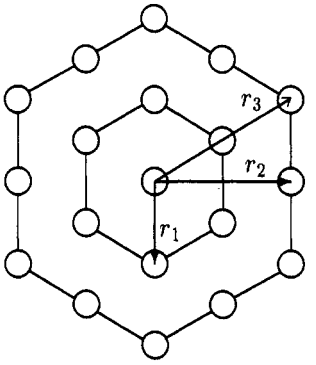

Figure 16. Shells of different neighbors of a given molecule. Three groups exist at distances r_1, r_2, r_3.

equal correlation factors are assumed for each group (C_1, C_2, C_3). $C(\mathbf{q})$ in eq 22 then can be transformed into[15]

$$C(q_\rho,\phi) = 1 + 6C_1[J_0(r_1q_\rho) + 2J_6(r_1q_\rho)\cos 6\phi] + 6C_2[J_0(r_2q_\rho) - 2J_6(r_2q_\rho)\cos 6\phi] + 6C_3[J_0(r_3q_\rho) + 2J_6(r_3q_\rho)\cos 6\phi]. \quad (23)$$

The curves shown in Figure 15 present the diffuse scattering averaged over ϕ, $S_D(q_\rho) = \langle S(q_\rho,\phi)\rangle$, calculated for different values of C_1 setting $C_2 = C_3 = 0$. For vanishing correlations, $C_1 = 0$, $S(q_\rho) \sim J_1^2$ shows the broad maximum of $J_1(q_\rho)$. Correlations result in a shift of the maximum towards the location of the Bragg reflection, together with a sharpening of the intensity distribution. The effect is quite clear and can be used for an analysis of the defect structure in PTFE base on a measurement of the diffuse scattering.

Figure 17 presents in a schematic drawing the scattering function of a PTFE crystal as it is found in the intermediate phase. The pattern shows Bragg reflections, as well as diffuse streaks oriented along the layer lines, and is set up by J_0 contributions (equator and meridian region) and J_1 contributions (torus range).

Scattering Function of a PTFE-Molecule with Helix-Reversal Defects. As it was shown first by Corradini and Guerra,[10] using straightforward numerical calculations, helix-reversal defects in a PTFE chain modify the intensity distribution in the torus region in a characteristic way. We have now used a general correlation function approach for model calculations and the analysis of measured data.

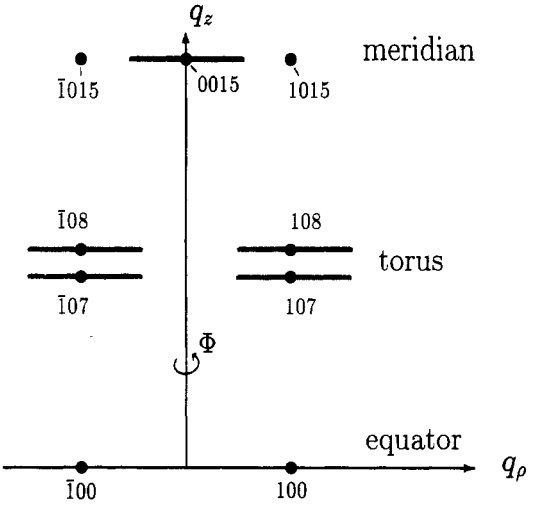

Figure 17. Scattering pattern of PTFE in the intermediate and high-temperature phase, with three specific ranges: equator, torus, and meridian. Schematic drawing.

The scattering function of a PTFE molecule with helix-reversal defects can be derived from the molecular-structure factor F_m by taking an average over all conformational and orientation states:

$$S(q) = \langle |F_m|^2 \rangle$$

Since the torus region is dominated by the J_1 contributions, F_m is given by (compared to eq 1)

$$F_m(q_\rho,\phi,q_z) \approx iJ_1(q_\rho r_l)\exp(i)\phi \cdot \cos\beta \sum_{l=1}^{N} \exp(i)(z_l q_z + \varphi_l) - iJ_{-1}(q_\rho r_l)\exp(-i)\phi \cdot \cos\beta \sum_{l=1}^{N} \exp(i)(z_l q_z - \varphi_l) \quad (24)$$

The 2-fold averaging (firstly over ϕ, accounting for the rotation) gives

$$\langle F_m F_m^* \rangle = \cos^2\beta J_1^2 \sum_{l,l'} \{\langle \exp(i)[(z_l - z_{l'})q_z + (\varphi_l - \varphi_{l'})]\rangle + \langle \exp(i)[(z_l - z_{l'})q_z - (\varphi_l - \varphi_{l'})]\rangle\} = \cos^2\beta J_1^2 \sum_{l=1}^{N-1} (N-l)\{\langle \exp(i)(\Delta z_l q_z + \Delta\varphi_l)\rangle + \langle \exp(i)(\Delta z_l q_z - \Delta\varphi_l)\rangle + \mathrm{CC}\} = \cos^2\beta J_1^2 \sum_{l=1}^{N-1} (n-1) \{\langle \exp(i)\chi_l\rangle + \langle \exp(i)\bar{\chi}_l\rangle + \mathrm{CC}\} \quad (25)$$

(CC designates the complex conjugate). Here Δz_l and $\Delta\varphi_l$ denote the longitudinal and angular displacements between two monomers at a distance l along the chain; χ_l and $\bar{\chi}_l$ give the phase differences of the scattered waves.

For a perfect helix χ_l and $\bar{\chi}_l$ increase linearly with l:

$$\chi_l \sim l, \quad \bar{\chi}_l \sim l \quad (26)$$

Perturbations of the helix by reversal defects in general result in random fluctuations of χ_l. The values of χ_l become distributed about a certain average value. In general, the width of the distribution will increase together with the decrease l. Simple analytical results are obtained if a Gaussian distribution is assumed with a variance

$$\langle \Delta\chi_l^2 \rangle = \langle \Delta\chi_0^2 \rangle \cdot l, \quad (27)$$

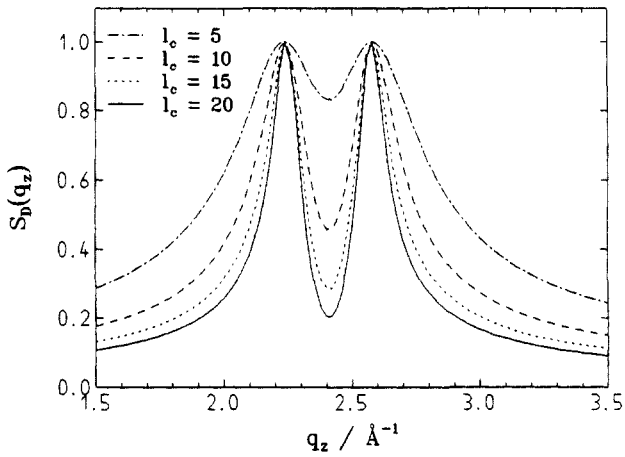

Figure 18. Scattering intensity distribution along q_z in the torus range, calculated for a model, assuming different values for the twist correlation length l_c.

and a mean value

$$\langle \chi_l \rangle = (\Delta z q_z + 2\pi t/u) l \tag{28}$$

which corresponds to the unperturbed helix.

This leads to

$$\langle \exp(i)\chi_l \rangle = \exp\left(-\frac{1}{2}\right) \langle \Delta\chi_l^2 \rangle \cdot \exp(i) \langle \chi_l \rangle$$
$$= \exp[-(l/l_c)] \cdot \exp(i) l (\Delta z q_z + 2\pi t/u) \tag{29}$$

with

$$l_c = 2/\langle \Delta\chi_0^2 \rangle \tag{30}$$

The parameter l_c describes the twist-correlation length. For perturbed chains azimuthal angles are only correlated over a finite number of units in the order of $l \approx l_c$. Equivalently it is

$$\langle \exp(i)\bar{\chi}_i \rangle = \exp[-(l/l_c)] \cdot \exp(i) l (\Delta z q_z - 2\pi t/u) \tag{31}$$

Insertion of eqs 29 and 31 into eq 22 yields an expression for $S_D(\mathbf{q})$, which includes l_c as an unknown parameter, together with the basic helix parameters Δz and t/u:

$$S_D(\mathbf{q}) \sim J_1^2 \sum_{l=1}^{N-1} (N-1) \exp(-l/l_c) \cdot \{\cos l(\Delta z q_z + 2\pi t/u) + \cos l(\Delta z q_z - 2\pi t/u)\} \tag{32}$$

Figure 18 presents the results of model calculations, performed on the basis of eq 32 for different values of l_c. A decrease of l_c, as would result from an increase of the concentration of helix-reversal defects, leads to a broadening of the two layer lines in the torus range. At sufficiently high concentrations, they merge together. As will be shown in the following, scattering data in the high-temperature phase can be well represented by eq 32. Curve adjustment then gives the twist-correlation length l_c together with the helix parameters u/t and Δz.

States of Disorder in the Intermediate Phase and the High-Temperature Phase of PTFE. Consideration of the general appearance of the scattering patterns and the changes observed in the two phase transitions allows some definite conclusions to be drawn concerning the defect structure in the intermediate and high-temperature phase.

Intermediate Phase (Modification IV). The disappearance of several reflections and also of complete layer lines (Figure 1) is indicative for a breakdown of the superlattice present in the low-temperature modification. The (triclinic) low-temperature phase is made up of arrays of right- and left-handed helices in alternate order.[22] Obviously this order, which produces the superlattice, gets lost at the phase transition. In the intermediate phase right- and left-handed helices become mixed; a long-range order in the occupation of lattice points with the two helical species no longer exists.[23]

As shown by the Bragg reflections in the meridian range, there is a positional long-range order of the CF_2 units in three dimensions.

There is also a three-dimensional orientational long-range order. Preferred orientations exist for each CF_2 group. This is clearly shown by the existence of the 107 and the 108 reflection in the intermediate phase.

On the other hand, there is also direct evidence for a pronounced disorder, in addition to the mixing of right- and left-handed helices. The diffuse streaks showing up on the layer lines in the torus range (Figure 1) are indicative for larger orientational displacements of the CF_2 units. The diffuse streak along the layer line in the meridian region indicates longitudinal displacements of the chains. In addition, the IR and Raman spectra (Figures 7 and 9) provide evidence for the occurrence of conformational defects in the chains. The proposition of previous authors to assign the defect bands to helix-reversal defects is strongly supported by the observed broadening of the layer lines in the torus range. As already pointed out in the previous chapter, the temperature dependence of the spectra (Figures 8 and 10) indicates a sharp increase in the concentration of the helix-reversal defects on passing through the intermediate phase.

Hence, in the intermediate phase one finds a 3d long-range order in the orientational and positional degrees of freedom of the CF_2 units, together with a pronounced disorder. At first view, an orientational long-range order in the presence of helix-reversal defects is surprising. Helix-reversal defects in general lead to a breakdown of the twist orientational long-range order for long parts of the helix. Such a breakdown, however, is not observed. We will present a possible solution of this problem in the following discussion.

High-Temperature Phase (Modification I). As demonstrated by the persistence of the Bragg reflections ((0 0 15) and (1 0 15)) at the layer line in the meridian region (Figure 1), the 3d-positional long-range order in the crystal is still retained. As shown by Yamamoto and Hara[24] these Bragg reflections exist up to 150 °C, where they disappear.

The disappearance of the Bragg reflections in the torus region tells that the orientational long-range order now has been completely destroyed. Reorientations of the monomer units cover uniformly the full 360° range, so that (eq 20)

$$\langle \exp(i)\delta\phi \rangle = 0$$

A reorientation of a complete chain sequence, which traverses a PTFE crystallite, in one step appears impossible. The activation energy for such a jump would be far too high (this is in contrast to the situation encountered for the oligomer $C_{20}F_{42}$, where jumps of the whole molecule have in fact been observed, and therefore a true rotator phase exists[15,17]). In the case of a PTFE chain incorporated in a crystallite, a reorientation can only be effected through the action of mobile effects like the helix-reversal defects.

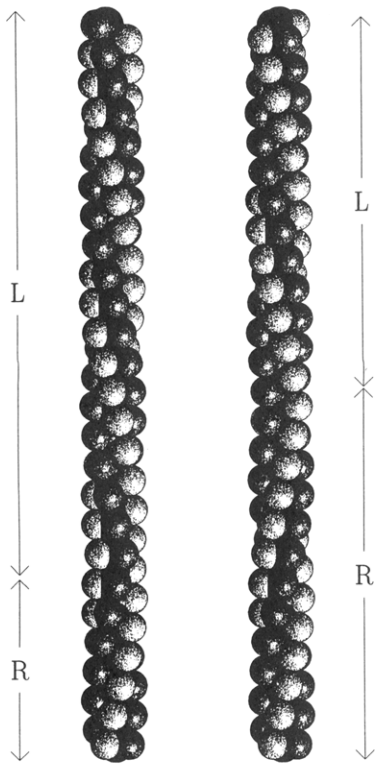

Figure 19. PTFE chain with a single helix-reversal defect. A shift of the defect necessitates a reorientation of all groups in the upper part of the chain.

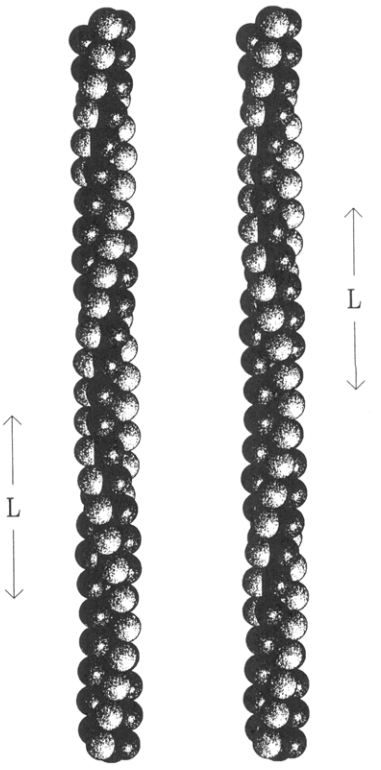

Figure 20. PTFE chain with a twin helix-reversal defect. A shift of the twin defect leaves the lower and upper part of the chain unaffected.

They constitute the dominant mechanism responsible for the observed reorientation of the CF_2 units in the crystallite.

However, there exist further requirements on the type of the defects. A single helix-reversal defect in a chain is rather immobile. Figure 19 sketches the situation and shows that an upward shift of the helix-reversal defect necessitates a turning of the whole upper chain sequence. This defect cannot move without a rearrangement of the orientation of long-chain sequences. As a consequence, and this has been shown also in a theoretical analysis by Heinonen and Taylor,[25] a single helix-reversal defect does not move with constant velocity. If it starts at one chain end, the velocity decreases on transporting the defect through the chain.

Much more probable, and this is our suggestion, is the occurrence of twin helix-reversal defects. A twin helix-reversal defect is sketched in Figure 20. It is clear that this is a true local perturbation of the chain and transport can be achieved without an effect on the chain ends. In contrast to the single helix-reversal defect, twin defects are truly soliton-like. They can move with a constant velocity along the chain.

A particular type of a twin defect is shown in Figure 21. It can be introduced in a chain without perturbing the original twist long-range order in the chain (the two right-handed sequences remain in register). Therefore, we shall call it a coherent twin defect. Its built up of a sequence of 15 units (or multiples of it), corresponding to the period of the helical chain.

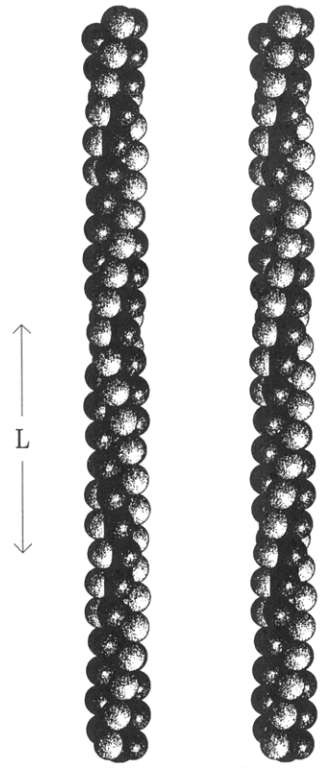

Figure 21. Unperturbed PTFE chain and chain which incorporates a coherent twin defect. Formation of this special defect does not destroy the twist long-range order of the helix.

Now we can come back to the previous problem to find a structure which possesses orientational long-range order, in spite of the presence of helix-reversal defects. Coherent twin defects show this property. The observation therefore suggests that they play a preferred role in the intermediate phase. Coherent twin defects can also produce the observed transformation of the helical sense. This could be envisaged as resulting from a successive formation and coupling of coherent twin defects. An example is given by the sketch in Figure 22.

The orientational long-range order gets lost at the phase transitions to the high-temperature phase. This breakdown, however, is not associated with a strong increase in the concentration of defects. There occurs only a small

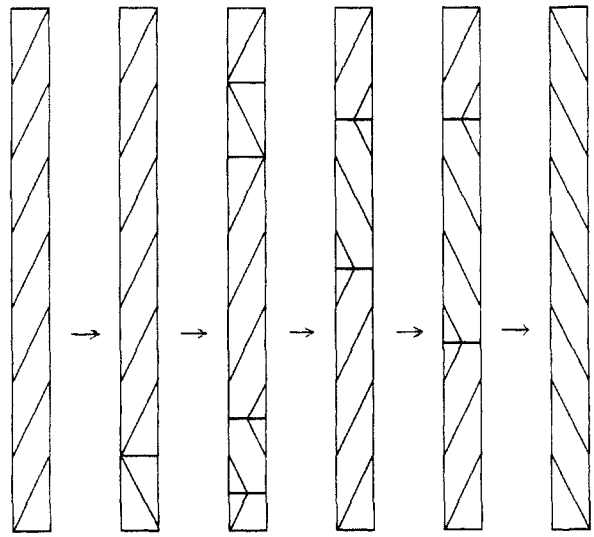

Figure 22. Transformation of a left-handed into a right-handed helix, realized by the successive formation, motion, and fusion of twin helix-reversal defects.

jump, if at all (Figures 4 and 10). At first view, this again looks quite surprising. However, starting from the picture developed for the intermediate phase based on the action of coherent twin defects, the resolution of the problem is simple: at the transition to the high-temperature phase the coherent character of the twin defects is lost. This can happen without a change in the defect concentration, just by a variation of the defect lengths in the high-temperature phase.

As already suggested in previous work by several authors,[8,10,11,26,27] the conformational state of a chain can now be described as a random sequence of right- and left-handed parts in alternate order. For such a chain an orientational long-range order no longer exists. For a given CF_2 unit a complete reorientation over 360° becomes possible as a result of the passing over of several twin defects.

A final comment concerns the observed temperature dependence of the defect concentration. An equilibration of the defect concentration has been indicated by Figures 8 and 10. No more changes were observed above 50 °C. The saturation value probably corresponds to the equilibrium value of defects in an individual stretched PTFE chain. The lower values found in the intermediate phase and at the begin of the high-temperature phase are determined by the additional effect of the lattice potential. At high temperatures this lattice potential is smeared out and no longer effective; here we essentially deal with a single-chain behavior. Hence, the steep increase in the defect concentration between the begin of the intermediate phase and the temperature range of about 50 °C can be understood as a transition from a state controlled by both intramolecular and intermolecular forces to one which is only determined by the intramolecular potentials.

It is interesting to note that in the high-temperature phase a short-range order in the orientation of the segments still exists. A quite similar observation has been made in our studies on the oligomer $C_{20}F_{42}$ in its rotator phase. The coefficient C_1 which characterizes the correlation in the orientations of neighboring chain sequences (eq 22) can be derived from the intensity distribution measured in the torus region along the layer lines. Figures 23 shows the results of a measurement performed on the thick film using X-ray scattering. Due to the imperfect orientation of the sample (a thick film), both layer lines contribute to the scattering intensity distribution. The two broken lines

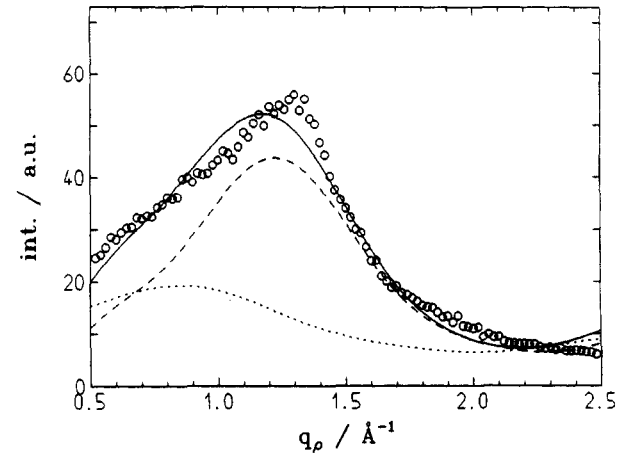

Figure 23. Intensity distribution along q_ρ, measured at T = 35 °C in an X-ray scattering experiment (q_z = 2.5 Å^{-1}, direction toward the Bragg position). Contributions of the two layer lines 107 (broken curve) and 108 (dotted curve) are superposed due to the imperfect orientation. The adjusted continuous curve was obtained assuming a correlation coefficient C_1 = 0.07.

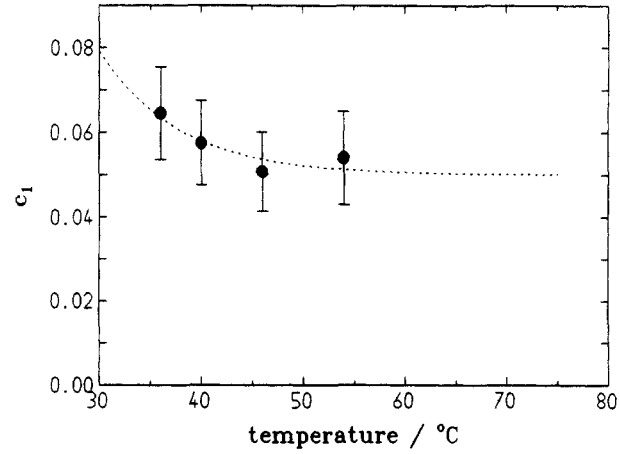

Figure 24. Temperature dependence of the correlation coefficient C_1 derived from the X-ray scattering experiments.

represent these two contributions. Both are determined by the correlation efficient C_1, which therefore can be derived from a curve fitting. The value of C_1 derived from the continuous curve in Figure 23, together with values obtained for measurements at higher temperatures, is presented in Figure 24. As shown by the values, the orientational correlation is weak, but it definitely exists. Here again, we find a first saturation at a temperature of 50 °C which indicates a coupling of the short-range order with the defect concentration. Of course, we would expect a decrease of the correlations with further increasing temperature. Investigations, however, have not been performed so far.

Twist Correlation Length of the Perturbed Helix. Calculations based on the model of the perturbed helix introduced in the previous chapter enable a determination of the twist correlation length l_c. Figure 25 presents as an example the intensity distribution along q_z in the torus region, obtained by a photometric recording of the electron diffractogram registered in the high-temperature phase at 40 °C. As shown by the calculated continuous curve, measured data are well represented by the introduced model. The calculated curve corresponds to a value l_c = 11 for the twist correlation length. By this an average length of the helical sequences of one sense in the order of 11 CF_2 units is indicated. The twist correlation length is generally related to the width in q_z direction of the layer lines in the torus range. Figure 26 shows the temperature

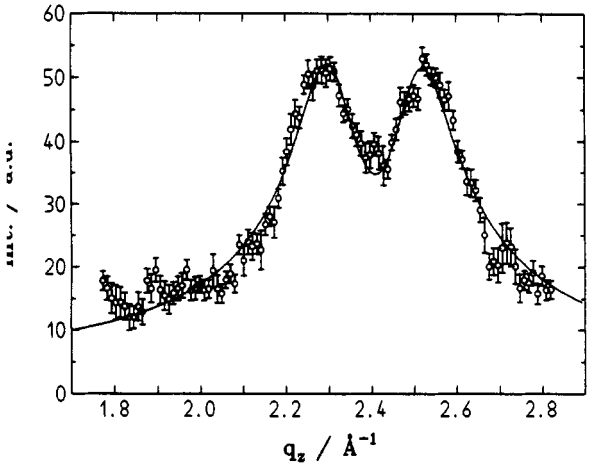

Figure 25. Intensity distribution along q_z, measured in the torus range at 40 °C (q_ρ = 1.30 Å^{-1}). The continuous curve represents the model calculations, assuming a twist-correlation length of 10.8 CF_2 units.

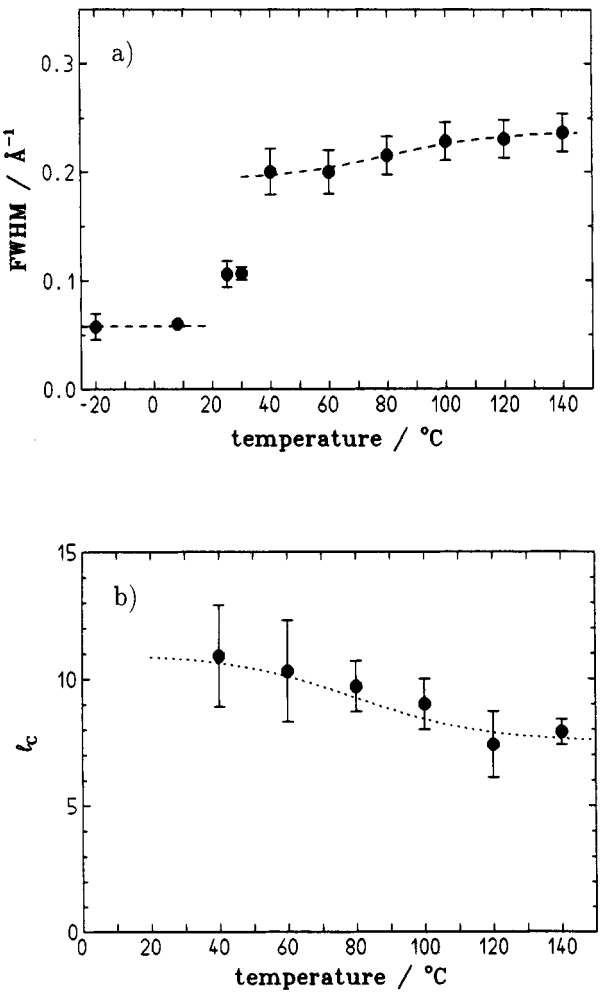

Figure 26. Results of the analysis of the q_z scans in the torus range. Temperature dependence of the width of the two layer lines and derived values for the twist-correlation length.

dependence of this width through all phases, together with values for the twist correlation length derived for the high-temperature phase (the model describes a perturbed chain without long-range order and therefore can only be applied to the high-temperature phase). Values for the twist correlation length in the high-temperature phase are found to lie in the range l_c = 8–11 and decrease with increasing temperature.

There is also clear evidence for a continuous effective unwinding of the helix, beginning in the intermediate

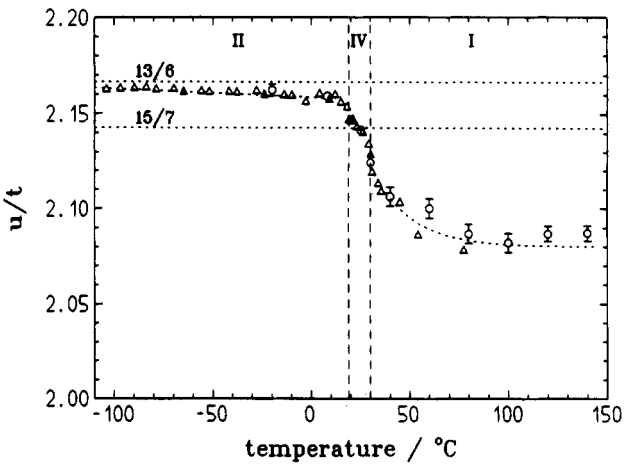

Figure 27. Temperature dependence of the helix parameter u/t, derived from the distance of the two layer lines in the torus range.

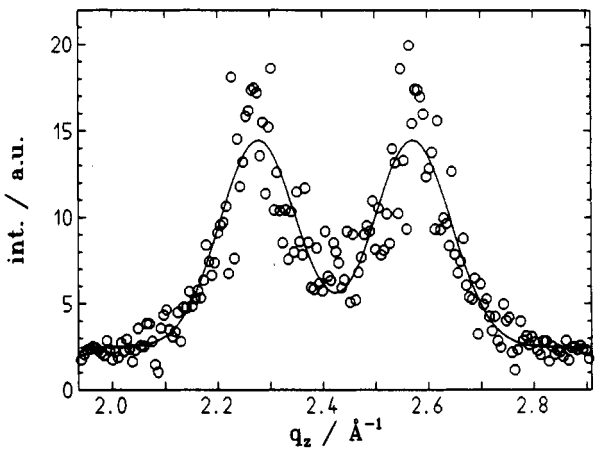

Figure 28. Scattering intensity distribution in the torus range obtained for a statistical model by numerical calculations. Representation of the simulated data by the analytical model.

phase, with particularly pronounced changes just after the phase transition into the high-temperature phase. This is shown in Figure 27. The helix parameter u/t is directly related to the distance between the two broadened layer lines. As it has been already shown in Figure 2, this distance decreases. Introducing the analytical model, the two quantities u/t and l_c were introduced as independent parameters. However, in reality they are coupled. The conformation of a single helix-reversal defect can be described by the sequence left-handed rotation (by 16.5°, starting from trans)/trans conformation/right-handed rotation for three successive CC bonds. Therefore, with increasing concentration of helix-reversal defects, in the average an all-trans conformation is approached. We have checked the effect by numerical calculations of the structure factor of a perturbed helix. Helix-reversal defects were distributed at random along a 15/7 helix. Averaging was performed over 100 different realizations, for 600 CF_2 units. The only parameter in the calculation is the mean distance between adjacent defects. Figure 28 shows the result of the calculation for a mean value $\bar{l}$ = 21. The continuous curve presents the fit of the analytical model onto the simulated data. Figure 29 shows the results of the simulations, which were performed under variation of the parameter $\bar{l}$. As expected, a decrease of $\bar{l}$ becomes reflected in an increase of the halfwidth of the layer-lines. The interesting point is the dependence of the helix parameter u/t, derived from the distance between the two broadened layer lines, on $\bar{l}$. For values below $\bar{l}$ = 20, a decrease is observed which corresponds to the unwinding

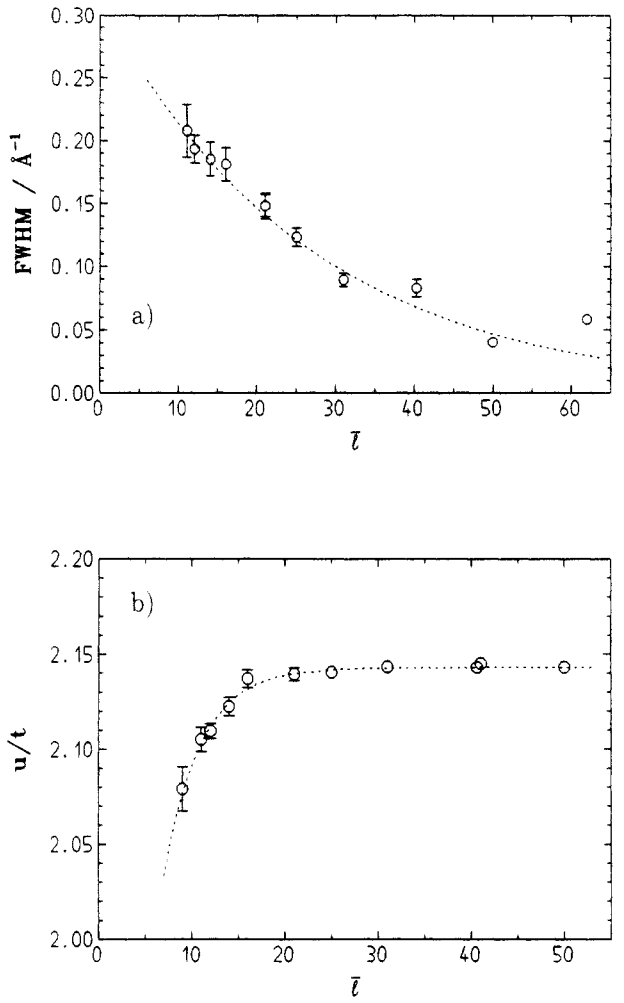

Figure 29. Relation between the helix parameter u/t and the average length of unperturbed helical sequences as derived from the simulations.

observed in the experiments. The results of the simulation are in reasonable agreement with the experiments. For $\bar{l}$ values in the order of 10 an effective unwinding is in fact predicted, with values in the range u/t = 2.08–2.12 as observed.

Evidence for Twin Defects. A common discussion of the results of the X-ray scattering experiments in the torus range and the Raman spectroscopic measurements provides further support for the suggested occurrence of coherent twin defect in the intermediate phase.

The intensity I_R of the defect induced band in the Raman spectrum is related to the concentration x of helix-reversal defects. Accounting for the effect of the amorphous phase, which gives a nonvanishing contribution I_R^0 already in the ordered low-temperature phase, it can be assumed

$$x \sim I_R - I_R^0 \tag{33}$$

An approximate value for the so far unknown proportionality constant can be derived from the results of the X-ray scattering experiments in the high-temperature phase. As explained in the previous chapter, here the mean length of the unperturbed sequences between successive helix-reversal defects is on the order of 10 monomer units (at 60 °C), which means

$$x \simeq 1/10 = 0.1$$

Using this for a calibration, the concentration of helix-reversal defects can be estimated using the equation

$$x(T) \simeq 0.1 \frac{I_R(T) - I_R^0}{I_R(60\ °C) - I_R^0} \tag{34}$$

The effect of the helix-reversal defects on the Bragg reflection intensities depends critically on the defect type. Generally the intensity of the Bragg reflections is determined by the fraction of long-range-ordered monomeric units in the chain. In the intermediate phase the orientation distribution function of a given unit can be described by

$$p(\varphi_l) = \alpha\delta(\varphi_l - \varphi_l^0) + (1-\alpha)/2\pi \tag{35}$$

The factor α gives the probability that a given unit is oriented in agreement with the twist long-range order along the helix. For the disordered units described by the second term we assume a uniform distribution. Bragg reflection intensities are given by the mean value of the structure factor:

$$I_{hkl} \sim |\langle F \rangle|^2$$

In the torus range the structure factor is essentially determined by the contribution of the Bessel function of order 1. The mean value then is given by

$$\langle F \rangle = (\text{const}) J_1 \sum_l \exp(i) z_l q_z \int_{\varphi_l} p(\varphi_l) \cdot \exp(i)\varphi_l \, d\varphi_l \tag{36}$$

$$= \alpha F^0 \tag{37}$$

Here F^0 denotes the structure factor of the unperturbed helix as it is measured in the low-temperature phase. Therefore, the decrease of the intensity of the Bragg reflection on the torus range, I_T, referred to the value in the low-temperature phase, I_T^0, gives the long-range order parameter α:

$$\frac{I_T}{I_T^0} = \frac{|\langle F \rangle|^2}{(F^0)^2} = \alpha^2 \tag{38}$$

The interesting point is a comparison between the fraction of disordered units, $1-\alpha$, and the concentration x of helix-reversal defects. For coherent twin defects one expects

$$1 - \alpha = 15 \cdot \frac{x}{2} = 7.5x$$

Single helix-reversal defects, on the other hand, have a much more destructive effect. In an average over all locations along the chain a single defect would destroy the long-range order for half of the monomer units of the chain sequence traversing the crystal, with length N

$$1 - \alpha \simeq \frac{N}{2} \cdot x$$

The experimental results give clear support for the twin defect. Let us look at the data observed in the center of the intermediate phase (25 °C). According to Figure 10 and eq 34 the defect concentration is approximately

$$x\ (25\ °C) \simeq 0.05$$

According to Figure 4b the fraction of long-ordered monomeric units is

$$\alpha(25\ °C) \simeq 0.75$$

Hence, we arrive at the ration

$$\frac{1-a}{x} \simeq 5$$

which is in good qualitative agreement with the value expected for the coherent twin defects. Individual defects certainly play no major role.

Reorientation Rates. According to the quasi-elastic neutron scattering experiments the reorientation of chain sequences in the high-temperature phase occurs with a rate in the order of 10–100 GHz (compare Figure 12, 1 meV = 240 GHz). Sequence reorientation results from the formation and motion of the twin helix-reversal defects. By this mechanism full turns over 360° can be realized. It is interesting to note that observed reorientation rates are comparable to the rotational diffusion constants measured for the oligomer $C_{20}F_{42}$.[17] This similarity makes sense, indeed. The length of the units in the PTFE chains which reorient has values in the order of 10, corresponding to the mean length of unperturbed sequences (Figure 26). This is comparable to the oligomer length. Considering that the lattice constants of PTFE and the oligomer $C_{20}F_{42}$ are equal (a = 5.70 Å), it is not surprising that similar values for the reorientation rates of the rotating oligomer molecules and the rotating chain sequences in PTFE are obtained.

The slowing down of the reorientation kinetics for q_ρ values near to the Bragg position (Figure 13) is a signature for correlations in the motion. The observation is in correspondence with the measurements of the static scattering function, where a maximum showed up at the same position (Figure 5). The maximum in the static structure factor originates from short-range-ordered clusters. These clusters stabilize the structure and decrease the reorientation rate of its constituents. Both the static and dynamic experiments suggest a decrease of the cluster size with increasing temperature (Figure 6 and 13), which comes as expected.

The libration frequences observed in the inelastic scattering experiment (Figure 14) again are comparable to the values found for the oligomer. In both cases the halfwidths lie in the range 1–2 meV. Obviously there is a broad spectrum of librational vibrations. The Gaussian central line used for the representation can be understood as the result of a superposition of many different modes. The vibrational character of these processes is indicated by the absence of any temperature dependence. Temperature only results in an increase of the vibration amplitude, i.e., in the integral intensity of these bands.

Conclusions

Scattering experiments with electrons, X-rays, and neutrons, together with vibrational spectroscopy, performed on biaxially oriented samples of PTFE suggest that the dominant mechanism of motion in the intermediate and high-temperature phase (modifications IV and I) is a reorientation of the chain units effected by the formation and motion of twin helix-reversal defects. In contrast to single helix-reversal defects these twin defects constitute a truly local perturbation, with solitonic dynamic properties. A twin defect can be shifted along the chain without affecting the other units. There is one species, the coherent twin defect, which possesses a particularly low activation energy. It corresponds to an alternate helical sequence with a length of 15 units equal to the period along the chain. Formation of a coherent twin helix-reversal defect retains the twist long-range order along the chain. Therefore the chain can stay with its unperturbed original parts in register with the surroundings. As a consequence there are only local contributions to the formation energy.

Formation of the defect occurs mainly in the intermediate phase. Then, in the high-temperature phase, an equilibrium is observed. The observations suggest a control of the defect concentration in the intermediate phase by both intra- and intermolecular potentials, and at high temperatures, when the intermolecular potentials are smeared out, a determination of the defect concentration by the intramolecular forces alone. The characteristic feature of the intermediate phase is the first formation of the twin defect at the phase transition, followed by a steep increase in their concentration. The twist long-range order is preserved through the intermediate phase, although it continuously decreases. The transition to the high-temperature phase is associated with a breakdown of the remaining orientational long-range order. The average length of helical sequences in on the order of 10 units. Dynamics can be envisaged as being essentially based on twin helix-reversal defects with no preference for the coherent species.

In contrast to the complete loss of orientational long-range order, CF_2 units still possess a positional long range order up to high temperatures. A 3d lattice thus is retained. The high-temperature phase is of plastic crystalline nature rather than being liquid crystalline.

Acknowledgment. Thanks are due to J. C. Wittmann (ICS Strasbourg) for his help and advice in the sample preparation. Support of the work by the Bundesminister für Forschung und Technologie is gratefully acknowledged.

References and Notes

(1) Bunn, C. W., Howells, E. R. *Nature 1954, 174*, 549.
(2) Franklin, R.; Klug, A. *Acta Crystallogr.* **1955**, *8*, 97.
(3) Pierce, H. H.; Clark, E. S.; Whitney, J. F.; Bryant, W. M. D. *Abstr. 130th Meet. Am. Chem. Soc.* **1956**, 9.
(4) Hirakawa, S.; Takemura, T. *Jpn. J. Appl. Phys.* **1969**, *8*, 635.
(5) Boeri, F. J.; Koenig, J. L. *J. Chem. Phys.* **1971**, *54*, 3667.
(6) Weeks, J. J.; Clark, E. S.; Eby, R. K. *Polymer* **1981**, *22*, 1480.
(7) Muus, L. T.; Clark, E. S. *Polymer Preprints* **1964**, *5*, 17.
(8) Brown, R. G. *J. Chem. Phys.* **1964**, *40*, 2900.
(9) Weeks, J. J.; Sanchez, I. C.; Eby, R. K.; Poser, C. I. *Polymer* **1980**, *21*, 325.
(10) Corradini, P.; Guerra, G. *Macromolecules* **1977**, *10*, 1410.
(11) Clark, E. S. *J. Macromol. Sci. Phys. B* **1967**, *1*, 795.
(12) Clark, E. S.; Muus, L. T. *Z. Krist* **1962**, *117*, 119.
(13) Wittmann, J. C.; Smith, P. *Nature* **1991**, *352*, 414.
(14) Schwickert, H.; Strobl, G.; Kimmig, M. *J. Chem. Phys.* **1991**, *95*, 2800.
(15) Albrecht, T.; Elben, H.; Jaeger, R.; Kimmig, M.; Steiner, R.; Strobl, G. *J. Chem. Phys.* **1991**, *95*, 2807.
(16) Albrecht, T.; Jaeger, R.; Petry, W.; Steiner, R.; Strobl, G.; Stühn, B. *J. Chem. Phys.* **1991**, *95*, 2817.
(17) Kimmig, M.; Steiner, R.; Strobl, G.; Stühn, B. *J. Chem. Phys.*, in press.
(18) Koenig, J. L.; Boerio, F. J. *J. Chem. Phys.* **1969**, *50*, 2823.
(19) Hannon, M. J.; Koenig, J. L.; Boerio, F. J. *J. Chem. Phys.* **1969**, *50*, 2829.
(20) Vainstein, B. K. *Diffraction of X-rays by Chain-Molecules*; Elsevier: Amsterdam, 1966.
(21) Guinier, A. *X-Ray Diffraction in Crystals, Imperfect Crystals and Amorphous Bodies*; W. H. Freeman: San Francisco, 1963.
(22) Farmer, B. L.; Eby, R. K. *Polymer* **1981**, *22*, 1487.
(23) Yamamoto, T.; Hara, T. *Polymer* **1986**, *27*, 986.
(24) Yamamoto, T.; Hara, T. *Polymer* **1982**, *23*, 521.
(25) Heinonen, O.; Taylor, P. L. *Polymer* **1989**, *30*, 585.
(26) De Santis, P.; Giglio, E.; Liquori, A. M.; Ripamonti, A. *J. Polym. Sci.* **1963**, 1383.
(27) Bates, T. W.; Stockmayer, W. H. *Macromolecules* **1968**, *1*, 12, 17.